Available online at www.sciencedirect.com

ScienceDirect

MATTER AND RADIATION AT EXTREMES

Matter and Radiation at Extremes 2 (2017) 296–302

www.journals.elsevier.com/matter-and-radiation-at-extremes

Research Article

A tabletop, ultrashort pulse photoneutron source driven by electrons from laser wakefield acceleration

X.J. Jiao [a,*], J.M. Shaw [a], T. Wang [a], X.M. Wang [a], H. Tsai [a], P. Poth [b], I. Pomerantz [a,c], L.A. Labun [a], T. Toncian [a], M.C. Downer [a], B.M. Hegelich [a]

[a] *Center for High Energy Density Science, University of Texas, Austin, TX 78712, USA*
[b] *Institut für Kernphysik, Technische Universität Darmstadt, Germany*
[c] *The School of Physics and Astronomy, Tel-Aviv University, Tel-Aviv, 69978, Israel*

Received 6 July 2017; revised 20 September 2017; accepted 26 October 2017
Available online 21 November 2017

Abstract

Relativistic electron beams driven by laser wakefield acceleration were utilized to produce ultrashort neutron sources. The experiment was carried out on the 38 fs, ~0.5 J, 800 nm Ti:Sapphire laser in the 10 TW UT^3 laser lab at University of Texas at Austin. The target gas was a high density pulsed gas jet composed of 90% He and 10% N_2. The laser pulse with a peak intensity of 1.5×10^{18} W/cm^2 interacted with the target to create a cylindrical plasma channel of 60 μm radius (FWHM) and 1.5 mm length (FWHM). Electron beams of ~80 pC with the Gaussian energy distribution centered at 37 MeV and a width of 30 MeV (FWHM) were produced via laser wakefield acceleration. Neutron fluences of ~2.4×10^6 per shot with hundreds of ps temporal length were generated through bremsstrahlung and subsequent photoneutron reactions in a 26.6 mm thick tungsten converter. Results were compared with those of simulations using EPOCH and GEANT4, showing agreement in electron spectrum, neutron fluence, neutron angular distribution and conversion rate.

PACS Codes: 29.25.Dz; 52.38.Kd; 52.38.Ph; 52.59.-f

Keywords: Neutron source; LWFA; Photoneutron reaction

1. Introduction

High fluence neutron sources are typically produced either by fission reactions in nuclear reactors or by spallation reactions [1], in which a high-energy proton beam impinges on a heavy metal target and ejects neutrons from the resulting excited nuclei. While these sources do produce high neutron flux, they are huge, costly and sometimes even policy-restricted [2], resulting in limited availability around the world [2]. The development of tabletop particle sources based on high intensity lasers has opened a window for laser plasma neutron source research [3–5]. Laser-based neutron sources are of special interest because the laser plasma interaction has an acceleration gradient thousands of times greater than conventional accelerators [6], giving these sources the potential to be compact and portable. Laser-based neutron sources are also versatile: from the same laser facility, users can obtain high energy electron beams [7], ion beams [6], X-rays [8] and neutrons [9], all with unique applications in industry and research. Additionally, laser-driven neutron sources have very short temporal structure and high peak fluence [9]. These features are favored by many applications that use pulsed neutron sources, such as fast neutron resonance radiography [10].

* Corresponding author.
E-mail address: jiao@utexas.edu (X.J. Jiao).
Peer review under responsibility of Science and Technology Information Center, China Academy of Engineering Physics.

https://doi.org/10.1016/j.mre.2017.10.003

Three typical schemes have been designed to create neutrons from laser plasma interactions. The first scheme is using a laser-accelerated ion beam (usually proton or deuterium via a target normal sheath acceleration or breakout afterburner mechanism) [6,11] to impinge on a converter made of a material with a high cross section for neutron production [12–25] (e.g. beryllium or lithium). The second scheme is using a high intensity laser to trigger fusion reactions in a deuteron target like that in inertial confinement fusion [3,26]. The third scheme is to irradiate the converter with high energy electron beams from laser wakefield acceleration (LWFA) [27] or direct laser acceleration, in which neutrons are generated through bremsstrahlung and photoneutron reactions [9,28–31]. In this work, neutron yield was optimized using the last scheme by varying the gas content and density of the gas target and material of the converter. This work was performed on the TW class 800 nm laser in the UT^3 laser lab at University of Texas at Austin.

2. Experimental setup

The experimental setup utilizes the laser–plasma interaction to create relativistic electrons, which are incident on a tungsten converter and radiate γ-rays through bremsstrahlung radiation. High energy γ-rays (>10 MeV) can interact with nuclei to produce neutrons. To generate LWFA, a 38 fs, ~0.5 J, linearly polarized laser pulse was focused to a spot size of ~17 μm (FWHM) with a peak intensity of ~1.5×10^{18} W/cm^2. The energy and fluence of the electron beams that were suitable for maximizing neutron production were controlled by the plasma density, which was in turn controlled by the gas type and density. The experiment ran at 2 shots/min due to the capability of the turbo pump (200 shots per measurement).

Fig. 1 shows the chamber layout. The main beam enters from the right side of the chamber and is focused on the gas target through an F/12.5 off-axis parabola. The gas jet nozzle has a 3 mm × 1 mm rectangular opening with 1 mm axis aligned with the laser propagation direction. The focusing position was determined by a thin metal wire taped at the front edge of the gas jet. The gas target was composed of 90% He and 10% N_2 to provide more electron injection in LWFA. A transverse interferometer measured the plasma density profile. The probe beam used for the plasma interferometer was separated from the main beam before entering the chamber and sent in through another window. Either a tungsten converter or a magnetic electron spectrometer was placed on the beam axis after the gas jet target. The magnetically dispersed electrons in the electron spectrometer were imaged by a LANEX screen and recorded by a CCD camera. The electron spectrometer measured electron energies of 10–50 MeV. Five bubble detectors [32] were deployed around the chamber as shown in Fig. 1, which were used to measure the neutron fluence. Bubble detectors were composed of droplets of superheated liquid. Neutrons deposited energy in the bubble detector through elastic collisions with nuclei and caused droplets to vaporize and form bubbles. The bubble detector was not sensitive to γ-rays, hence it was very suitable for this experiment. A neutron time-of-flight (n-TOF) was placed 2.18 m away from the converter and at 50° from laser propagation direction. The n-TOF was used to measure the neutron energy distribution. Fig. 1 illustrates how the n-TOF spectrometer works. The first part of the n-TOF was a plastic scintillator (EJ232), which emited light signals of certain wavelengths after being hit by neutrons. The signals were then amplified by a photomultiplier tube (XP2020) and recorded by a fast oscilloscope.

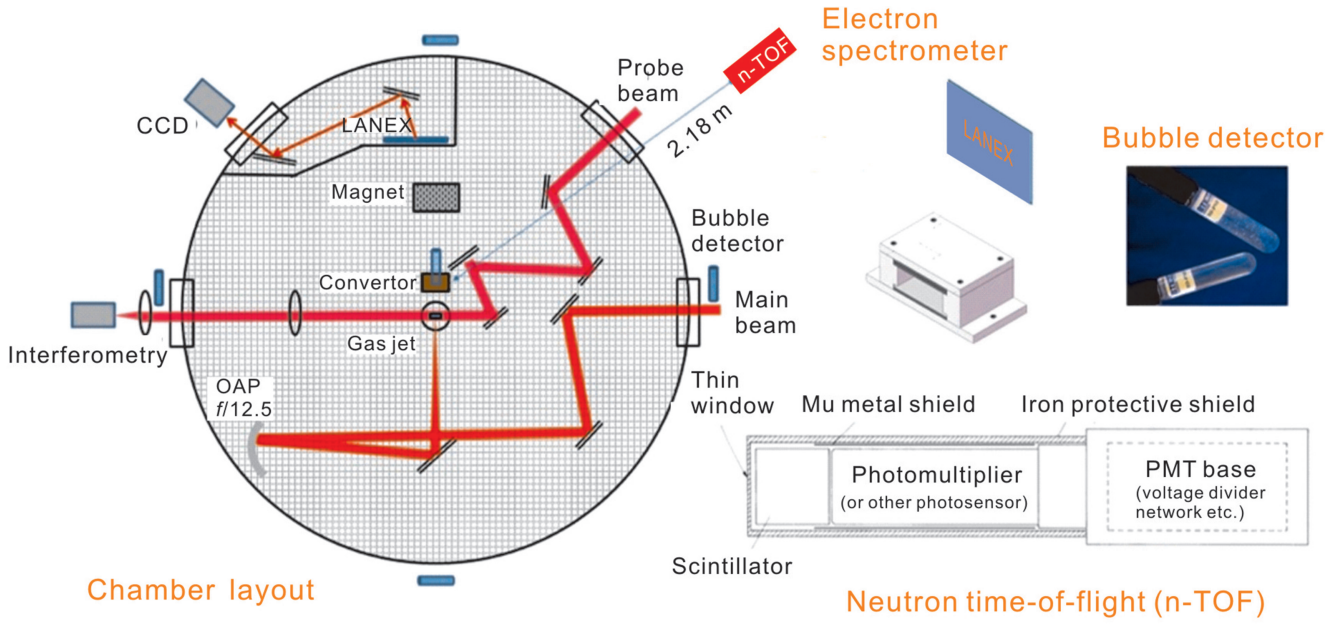

Fig. 1. Chamber layout of the experiment and diagnostic illustrations: electron spectrometer, bubble detectors, neutron time-of-flight detector.

3. Experimental results

Plasma density was recorded for all shots to help optimizing the electron beam. The plasma density profiles were consistent from shot to shot under the same target and laser conditions. The laser was focused on the front edge of the gas jet and created a cylindrical plasma channel of 60 μm in radius and 1.5 mm in length (FWHM). Fig. 2 is the typical plasma density measured when generating neutrons, including the source image as well as the calculated final density profile. The phase shift was calculated by comparing the source fringe with the background and then, the density profile was extracted, by Abel inversion.

The electron beam generated through LWFA in this experiment had low divergence with FWHM of 30 mrad, which made an online electron measurement impossible. The electron beam properties were analyzed and optimized before the converter was inserted. Fig. 3(a) shows the electron spot intensity map. A Gaussian fit estimates the electron beam divergence (Fig. 3(b)). Fig. 3(c) is the averaged electron energy distribution from the electron spectrometer and Fig. 3(d) is the LANEX intensity image. The electron energy has an approximately Gaussian distribution with energy peak at 37 MeV and width of 30 MeV (FWHM).

A 2D particle-in-cell simulation was performed with EPOCH [33] code to investigate the acceleration mechanism. In the simulation, a Gaussian pulse of the same parameters propagated through a trapezoid-shape plasma profile with the maximum density of $3.5 \times 10^{19}/\mathrm{cm}^3$. Fig. 4 (a) shows the electron spectrum, which resembles a superposition of an exponential decay at low energy and some tens of MeV peaks. Due to the limitation of our electron spectrometer, the low energy tail was not recorded, but the high-energy part was found to be qualitatively in agreement with the simulation. Fig. 4 (b)-(d) reveals the evolution of the interaction. The normalized vector potential a_0 was ~0.8, indicating a mildly nonlinear interaction at first. After that, the laser underwent a self-focusing process, resulting a much bigger a_0 , and eventually brought the interaction into a highly non-linear broken-wave regime [34]. The wave breaking happened at 2.7 ps and electrons trapped in the first wave bucket was accelerated up to 60 MeV. It should be noted that although the ratio between

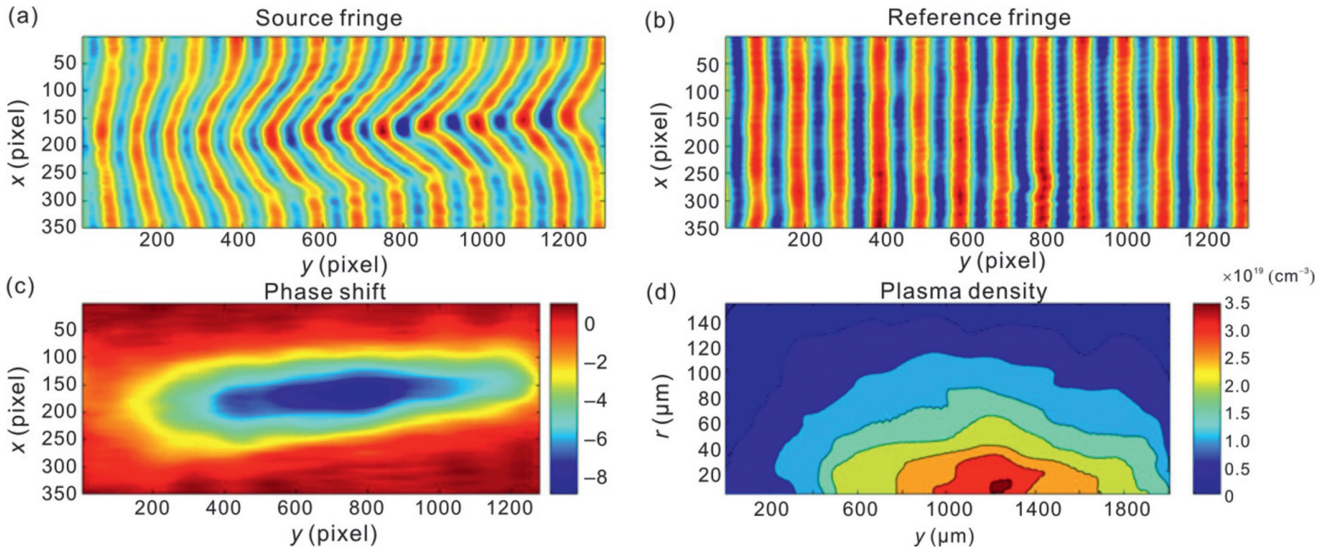

Fig. 2. (a) Fringe image detected on shot; (b) Background fringe; (c) Phase shift calculated from fringe image; (d) Contour plot of plasma density.

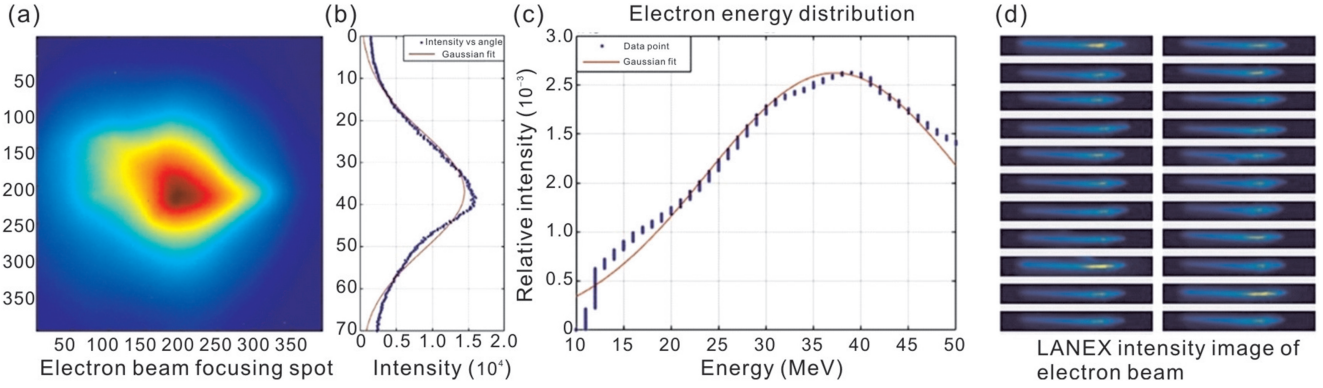

Fig. 3. (a) Electron beam size and (b) Gaussian fit on divergence profile; (c) Average electron energy distribution and (d) LANEX intensity image.

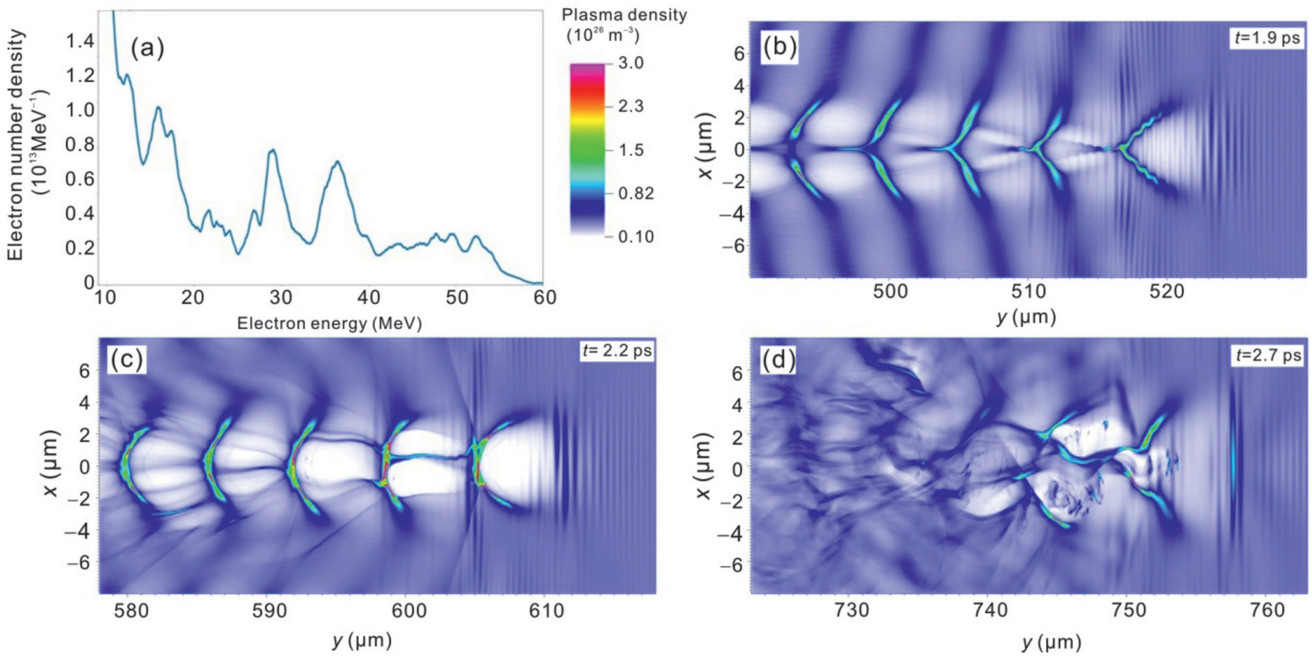

Fig. 4. (a) Electron spectrum from the simulation. (b)–(d) Electron density snapshots for t = 1.9ps, 2.2 ps, and 2.7ps during the 2D PIC simulation.

laser pulse length and the plasma wavelength λ_p was 2, self-modulated wakefield was not observed in the simulation.

The neutron fluence was measured by 5 bubble detectors placed outside the chamber at 0°, 90°, 90° (at the top of chamber), 180° and 270° with respect to the laser/electron propagation direction with respective distances of 50, 60, 46, 69 and 60 cm from the converter target. Fig. 5(a) shows the neutron fluence angular distribution. The horizontal axis shows the angle from laser propagation direction, the vertical axis shows neutron fluence in units of neutron number per steradian. The bubble detector set at the top of the chamber is at 90° in the plot and its data is very consistent with that of the detector on the side.

A nearly isotropic neutron fluence, except the front direction, was observed. The much higher front fluence signal was due to some of the γ-ray passing through the converter creating an additional source of electrons via Compton scattering and pair production in the chamber wall. The forward bubble detector was very close to this electron source; thus, it was subject to a large fluence of direct electrons. It appeared to be sensitive to these electrons. More discussion will be given on this topic in the subsequent GEANT4 simulation section. We could avoid this problem and increase the neutron yield by using a thicker converter, but it would inevitably reduce the available neutrons and surface fluence due to absorption in the converter and a big surface area. Data collected at other

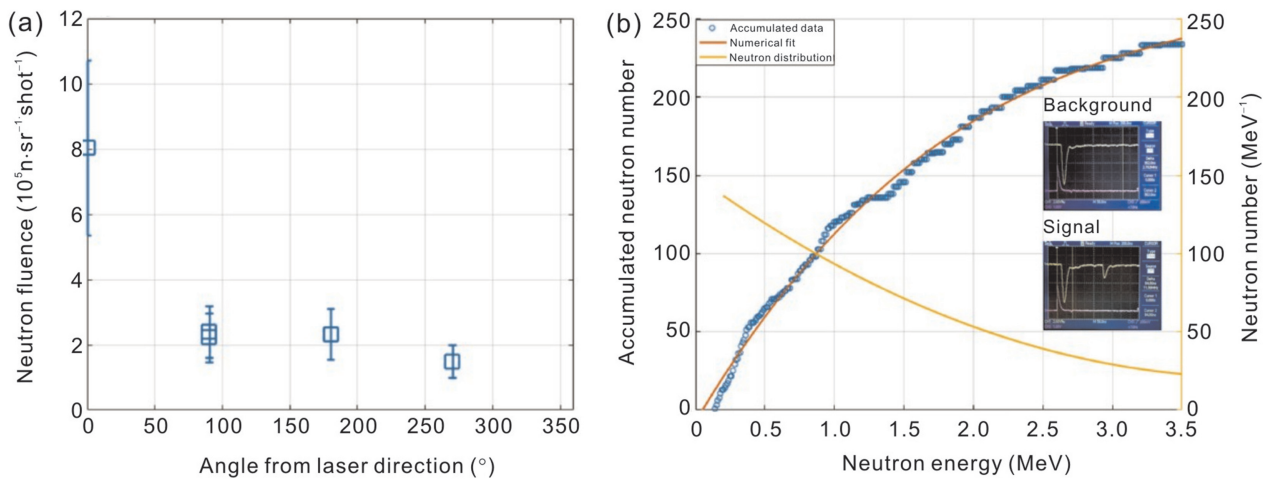

Fig. 5. (a) Neutron fluence angular distribution; (b) Neutron energy distribution, averaged over 200 shots. The inset pictures are oscilloscope waveforms of background and neutron signal.

positions, which were not affected by γ-rays, demonstrate neutron fluence of $>2 \times 10^6$ neutrons per shot, a result higher than that of the previous experiments [28,30] on comparable laser systems. Fig. 5(b) shows the neutron energy distribution. Detecting neutron energy is challenging and commonly done using time of flight method, which requires detectors to be set far away from the neutron source to accurately resolve the neutron energy. Because this practice also drastically reduced the signal level, we accumulated 200 shots during the experiment using an n-TOF signal spread from 100 to 400 ns to determine the energy distribution. The energy distribution was calculated by differentiating the numeric fit of the accumulated signal. The average number of neutrons detected on each shot was approximately 1.2, obtained from the oscilloscope waveform counting. This average number matches well with the total neutron fluence implied by the bubble detectors. In Fig. 5(b), the blue circles show the accumulated neutron number received at the scintillator, and the red line is the numerical fit to this data, which is then used to derive the energy spectrum, shown in yellow.

4. GEANT4 simulation results

To better understand the physics processes and optimize the neutron yield for future experiments, GEANT4 simulations [35] were carried out using the measured electron energy distribution from the experiment, aluminum target chamber, 26.6 mm tungsten converter and two detector rings centered at the converter—one inside the chamber and the other outside the chamber. The detector rings were used to study the angular distribution of escaping electrons, γ-rays and neutrons. The detection thresholds were set to be 5 MeV for both electrons and γ-rays. For tungsten, the photoneutron cross section falls to zero when the photon energy is less than 5 MeV. The electron beam, sampled with Gaussian energy distribution centered at 37 MeV with $\sigma = 13$ MeV, was launched towards the converter from the center of the chamber. The angular distribution of electrons was also set to have a Gaussian profile of 30 mrad FWHM to match the electron beam property measured. The simulation was done with 10^8 particles, corresponding to 16 pC electron bunches, about 20% of the electrons we measured as generated in each experimental shot.

Fig. 6 shows the reaction region for each physics process in the simulation. All color images are plotted on a log scale and normalized so that the highest value is a thousand times bigger than the lowest one. Fig. 6 (a) is the projection of electron energy deposition on the converter. The converter is thick enough to stop most of the electrons from penetrating. Fig. 6 (b) is the projection of γ-ray production due to Bremsstrahlung radiation. The production of γ-rays peaks at the front surface, then decreases with increasing depth and forms a shape like a candle flame, similar to the electron energy deposition. The radiation lengths for electrons and photons do not overlap, because the production of high energy gamma-rays occurs predominantly in the first 5 mm of the converter. This is in agreement with the fact that Bremsstrahlung radiation dominates above 20 MeV and its cross-section decreases as electron energy decreases, while energy loss due to collisions remains nearly constant. As electrons penetrate deeper, their energy decreases and more energy goes to ionization than γ-ray production. Because the detection threshold is set to be 5 MeV, the simulation also implies that the electrons lose their capability to create high energy γ-rays after 15 mm, therefore they do not contribute to generating neutrons. Image Fig. 6(c) is the projection of the total γ-ray scattering, which includes pair production, Compton scattering and photo-nuclear activation. The "cut off" on the projection contour implies a "leakage" of γ-rays. Compared with electrons, γ-ray leakage is much more severe, which we believe is the main reason for the exaggerated neutron signal collected at the front direction. Comparing Fig. 6(b) and (c) shows that while most γ-rays are created at the front surface, γ-ray scattering happens much deeper in the converter. There is, on average, a delay

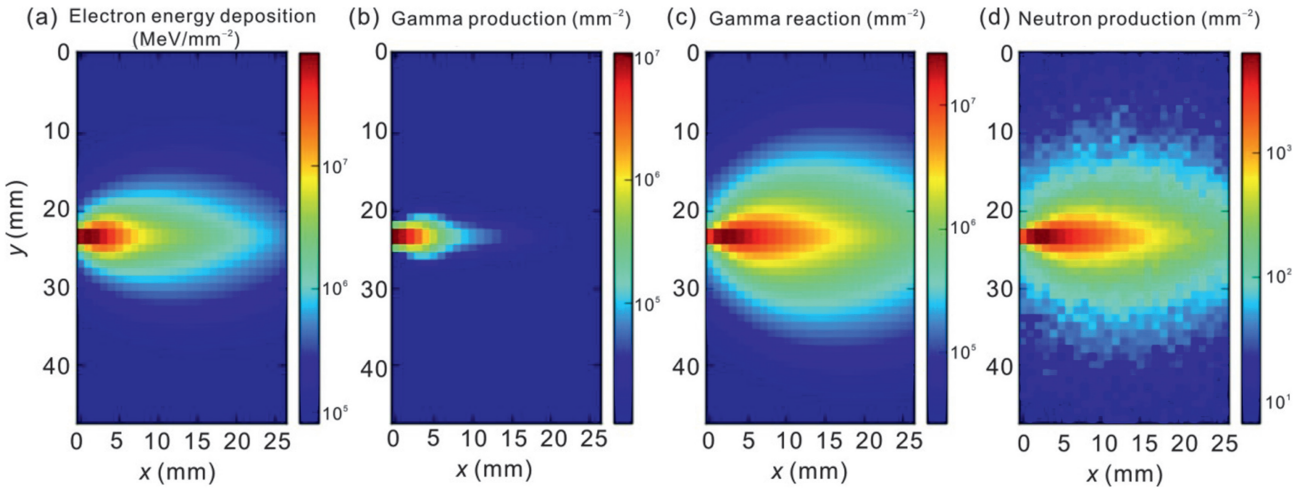

Fig. 6. Projection plot of reaction inside the converter. Numbers were integrated along the hidden axis and then normalized with the highest value is 1000 times the lowest. (a) Electron energy deposition indicates how much energy was deposited in certain location; (b) Projection plot of γ-ray (>5 MeV) production via bremsstrahlung radiation, in unit of number of gamma produced per mm^2; (c) γ-ray (>5 MeV) total scattering, which includes pair production, Compton scattering and photo-nuclear activation, in unit of number of reaction per mm^2; (d) Neutron produced via photo-nuclear reaction, in unit of number of neutron per mm^2.

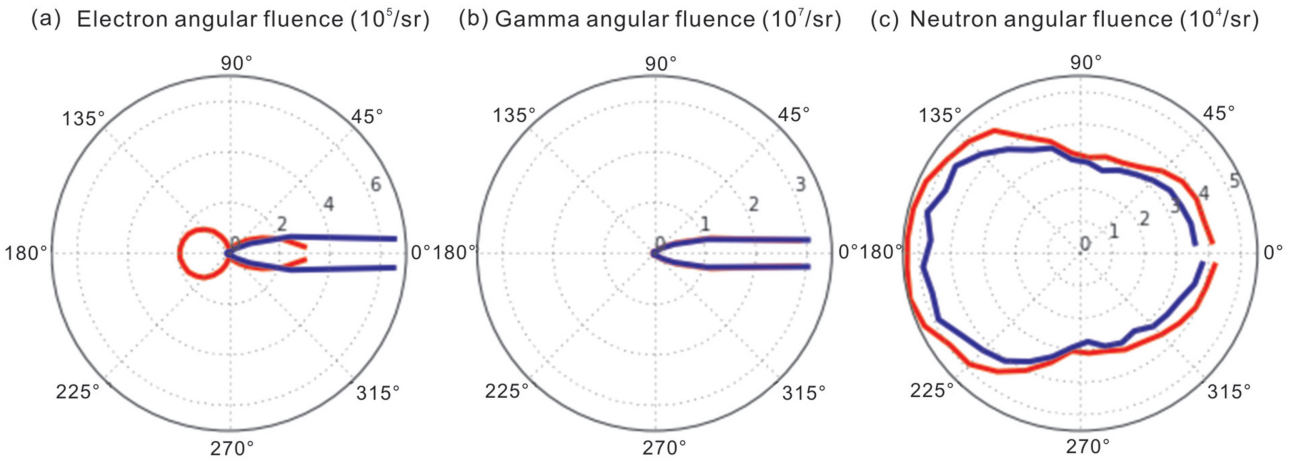

Fig. 7. (a) Electron angular fluence (>5 MeV); (b) γ-ray angular fluence (>5 MeV); (c) Neutron angular fluence. Red lines present the fluence detected inside the chamber, blue lines present the fluence detected outside the chamber.

between gamma production and gamma scattering which is approximately the mean free path of a gamma in tungsten. It suggests an efficient way to create a neutron source and collimated γ-ray source at the same facility simply by changing the thickness of the converter.

Fig. 7 shows the angular fluence distribution of the escaping electrons, γ-rays and neutrons. The 0° direction is the electron forward direction. The red lines present the data collected at the detector inside the chamber, the blue lines present the data outside the chamber. As we can see, both the escaping electrons and γ-rays went forward with a small divergence. Some electrons were scattered backward at the front surface and had a surface fluence following cosine law. Most electrons that escaped from the converter were absorbed by the chamber wall. The electrons detected by the outer detector were created by Compton scattering and pair production induced by escaping γ-rays with fluence two magnitudes greater than that of electrons. The neutrons, however, showed a nearly isotropic distribution, inside and outside the chamber, indicating that not many neutrons were created at the chamber wall. For this reason, we suspect that the bubble detector at 0° was affected by high energy electrons. Even though bubble detectors were claimed to be insensitive to γ-rays, they were not tested for their sensitivities to high energy electrons. Future experiments will be conducted to calibrate the bubble detector response to high energy electrons. The isotropic neutron fluence detected in other directions also supports this interpretation, as the escaping particles were well collimated, and bubble detectors in other direction were not affected. The average neutron fluence inside the chamber is 4×10^4/sr, which is also about 20% of the neutrons detected. The electron to neutron conversion efficiency is about 1/2500. Both agree very well with that of the experiment.

5. Conclusion

A neutron source with $>2 \times 10^6$ neutrons per shot was created by using LWFA on a TW class laser. The conversion efficiency from laser energy to neutrons is greater than 4×10^6 neutrons/J, higher than some previous results [3,19,21,23,24,28,30]. The conversion efficiency from electrons to neutrons is about 1/2500. In the experiment, the neutron pulse had a very short temporal structure of ~300 ps, which is estimated by the time that mean energy neutron bunches travel through the reaction region. The peak neutron emission rate was estimated to be 6.7×10^{16}/s. The efficiency can be further improved by optimizing converter geometry and changing converter material (e.g. uranium) as well as optimizing the energy distribution of the electron beam bunch. With upcoming high repetition kHz lasers, the neutron average flux can be improved as well, making this neutron source a prominent candidate for small applications such as neutron holography [36] and neutron resonance spectroscopy [22].

Acknowledgments

This paper is based upon work supported by the Air Force Office of Scientific Research under award number FA9550-14-1-0045. The project was also supported by the NNSA cooperative agreement DE-NA0002008, the Defense Advanced Research Projects Agency's PULSE program (12-63-PULSE-FP014). Simulations were performed using GEANT4 on Lonestar 5 cluster provided by the TACC at University of Texas at Austin.

References

[1] A. Taylor, M. Dunne, S. Bennington, S. Ansell, I. Gardner, et al., A Route to the brightest possible neutron source? Science 315 (2007) 1092–1095, https://doi.org/10.1126/science.1127185.
[2] H.Z. Bilheux, R. McGreevy, I.S. Anderson (Eds.), Neutron Imaging and Applications, Springer, US, Boston, MA, 2009, https://doi.org/10.1007/978-0-387-78693-3.
[3] T. Ditmire, J. Zweiback, V.P. Yanovsky, T.E. Cowan, G. Hays, et al., Nuclear fusion from explosions of femtosecond laser-heated deuterium clusters, Nature 398 (1999) 489–492.

[4] F. Albert, A.G.R. Thomas, S.P.D. Mangles, S. Banerjee, S. Corde, et al., Laser wakefield accelerator based light sources: potential applications and requirements, Plasma Phys. Control. Fusion 56 (2014) 084015, https://doi.org/10.1088/0741-3335/56/8/084015.

[5] F. Albert, A.G.R. Thomas, Applications of laser wakefield accelerator-based light sources, Plasma Phys. Control. Fusion 58 (2016) 103001, https://doi.org/10.1088/0741-3335/58/10/103001.

[6] A. Macchi, M. Borghesi, M. Passoni, Ion acceleration by superintense laser-plasma interaction, Rev. Mod. Phys. 85 (2013) 751−793, https://doi.org/10.1103/RevModPhys.85.751.

[7] E. Esarey, C.B. Schroeder, W.P. Leemans, Physics of laser-driven plasma-based electron accelerators, Rev. Mod. Phys. 81 (2009) 1229−1285, https://doi.org/10.1103/RevModPhys.81.1229.

[8] H.-E. Tsai, X. Wang, J.M. Shaw, Z. Li, A.V. Arefiev, et al., Compact tunable Compton X-ray source from laser-plasma accelerator and plasma mirror, Phys. Plasmas 22 (2015) 023106, https://doi.org/10.1063/1.4907655.

[9] I. Pomerantz, E. McCary, A.R. Meadows, A. Arefiev, A.C. Bernstein, et al., Ultrashort pulsed neutron source, Phys. Rev. Lett. 113 (2014), https://doi.org/10.1103/PhysRevLett.113.184801.

[10] I. Mor, D. Vartsky, D. Bar, G. Feldman, M.B. Goldberg, et al., High spatial resolution fast-neutron imaging detectors for Pulsed Fast-Neutron Transmission Spectroscopy, J. Instrum. 4 (2009), https://doi.org/10.1088/1748-0221/4/05/P05016. P05016−P05016.

[11] N. Guler, P. Volegov, A. Favalli, F.E. Merrill, K. Falk, et al., Neutron imaging with the short-pulse laser driven neutron source at the Trident laser facility, J. Appl. Phys. 120 (2016) 154901, https://doi.org/10.1063/1.4964248.

[12] M. Roth, D. Jung, K. Falk, N. Guler, O. Deppert, et al., Bright laser-driven neutron source based on the relativistic transparency of solids, Phys. Rev. Lett. 110 (2013), https://doi.org/10.1103/PhysRevLett.110.044802.

[13] M. Roth, D. Jung, K. Falk, N. Guler, O. Deppert, et al., A bright neutron source driven by relativistic transparency of solids, J. Phys. Conf. Ser. 688 (2016) 012094, https://doi.org/10.1088/1742-6596/688/1/012094.

[14] K.L. Lancaster, S. Karsch, H. Habara, F.N. Beg, E.L. Clark, et al., Characterization of ^{7}Li(p,n)7Be neutron yields from laser produced ion beams for fast neutron radiography, Phys. Plasmas 11 (2004) 3404−3408, https://doi.org/10.1063/1.1756911.

[15] D. Jung, K. Falk, N. Guler, O. Deppert, M. Devlin, et al., Characterization of a novel, short pulse laser-driven neutron source, Phys. Plasmas 20 (2013) 056706, https://doi.org/10.1063/1.4804640.

[16] C. Zulick, F. Dollar, V. Chvykov, J. Davis, G. Kalinchenko, et al., Energetic neutron beams generated from femtosecond laser plasma interactions, Appl. Phys. Lett. 102 (2013) 124101, https://doi.org/10.1063/1.4795723.

[17] W. Bang, M. Barbui, A. Bonasera, H.J. Quevedo, G. Dyer, et al., Experimental study of fusion neutron and proton yields produced by petawatt-laser-irradiated D 2-3 He or CD 4-3 He clustering gases, Phys. Rev. E 88 (2013), https://doi.org/10.1103/PhysRevE.88.033108.

[18] L. Disdier, J.-P. Garçonnet, G. Malka, J.-L. Miquel, Fast neutron emission from a high-energy ion beam produced by a high-intensity subpicosecond laser pulse, Phys. Rev. Lett. 82 (1999) 1454−1457, https://doi.org/10.1103/PhysRevLett.82.1454.

[19] M. Storm, S. Jiang, D. Wertepny, C. Orban, J. Morrison, et al., Fast neutron production from lithium converters and laser driven protons, Phys. Plasmas 20 (2013) 053106, https://doi.org/10.1063/1.4803648.

[20] G.M. Petrov, D.P. Higginson, J. Davis, T.B. Petrova, J.M. McNaney, et al., Generation of high-energy (>15 MeV) neutrons using short pulse high intensity lasers, Phys. Plasmas 19 (2012) 093106, https://doi.org/10.1063/1.4751460.

[21] D.P. Higginson, J.M. McNaney, D.C. Swift, T. Bartal, D.S. Hey, et al., Laser generated neutron source for neutron resonance spectroscopy, Phys. Plasmas 17 (2010) 100701, https://doi.org/10.1063/1.3484218.

[22] V.S. Belyaev, V.I. Vinogradov, A.P. Matafonov, V.P. Krainov, V.S. Lisitsa, et al., Neutron production in picosecond laser-generated plasma on a be target, Phys. At. Nucl. 69 (2006) 919−923, https://doi.org/10.1134/S1063778806060019.

[23] C.L. Ellison, J. Fuchs, Optimizing laser-accelerated ion beams for a collimated neutron source, Phys. Plasmas 17 (2010) 113105, https://doi.org/10.1063/1.3497011.

[24] D.P. Higginson, J.M. McNaney, D.C. Swift, G.M. Petrov, J. Davis, et al., Production of neutrons up to 18 MeV in high-intensity, short-pulse laser matter interactions, Phys. Plasmas 18 (2011) 100703, https://doi.org/10.1063/1.3654040.

[25] S. Karsch, S. Düsterer, H. Schwoerer, F. Ewald, D. Habs, et al., High-intensity laser induced ion acceleration from heavy-water droplets, Phys. Rev. Lett. 91 (2003), https://doi.org/10.1103/PhysRevLett.91.015001.

[26] X. Wang, R. Zgadzaj, N. Fazel, Z. Li, S.A. Yi, et al., Quasi-monoenergetic laser-plasma acceleration of electrons to 2 GeV, Nat. Commun. 4 (2013), https://doi.org/10.1038/ncomms2988.

[27] S.A. Reed, V. Chvykov, G. Kalintchenko, T. Matsuoka, V. Yanovsky, et al., Efficient initiation of photonuclear reactions using quasimonoenergetic electron beams from laser wakefield acceleration, J. Appl. Phys. 102 (2007) 073103, https://doi.org/10.1063/1.2787159.

[28] D.N. Gupta, H. Suk, Energetic electron beam generation by laser-plasma interaction and its application for neutron production, J. Appl. Phys. 101 (2007) 114908, https://doi.org/10.1063/1.2738377.

[29] W.P. Leemans, D. Rodgers, P.E. Catravas, C.G.R. Geddes, G. Fubiani, et al., Gamma-neutron activation experiments using laser wakefield accelerators, Phys. Plasmas 8 (2001) 2510−2516, https://doi.org/10.1063/1.1352617.

[30] I. Pomerantz, E. McCary, A.R. Meadows, A. Arefiev, A.C. Bernstein, et al., in: K.W.D. Ledingham, K. Spohr, P. McKenna, P.R. Bolton, E. Esarey, et al. (Eds.), Laser Generation of Ultra-short Neutron Bursts from High Atomic Number Converters, 2015, p. 95140Q, https://doi.org/10.1117/12.2181494.

[31] M.A. Buckner, Improving Neutron Dosimetry Using Bubble Detector Technology, Oak Ridge National Lab., TN (United States), 1993.

[32] T.D. Arber, K. Bennett, C.S. Brady, A. Lawrence-Douglas, M.G. Ramsay, et al., Contemporary particle-in-cell approach to laser-plasma modelling, Plasma Phys. control. Fusion 57 (2015) 113001, https://doi.org/10.1088/0741-3335/57/11/113001.

[33] A. Pukhov, J. Meyer-ter-Vehn, Laser wake field acceleration: the highly non-linear broken-wave regime, Appl. Phys. B Lasers Opt. 74 (2002) 355−361, https://doi.org/10.1007/s003400200795.

[34] J. Allison, K. Amako, J. Apostolakis, H. Araujo, P.A. Dubois, et al., Geant4 developments and applications, IEEE Trans. Nucl. Sci. 53 (2006) 270−278, https://doi.org/10.1109/TNS, 2006.869826.

[35] D. Sarenac, M.G. Huber, B. Heacock, M. Arif, C.W. Clark, et al., Holography with a neutron interferometer, Opt. Express 24 (2016) 22528−22535, https://doi.org/10.1364/OE.24.022528.